

1 On the use of Li isotopes as a proxy for water-rock interaction in
2 fractured crystalline rocks: a case study from the Gotthard rail
3 base tunnel

4 **Christoph Wanner^{1*}, Kurt Bucher², Philip A. E. Pogge von Strandmann³, H. Niklaus
5 Waber¹, Thomas Pettke¹**

6 *¹Rock Water Interaction Group, Institute of Geological Sciences, University of Bern,
7 Baltzerstrasse 3, CH-3012 Bern, Switzerland.*

8 *²Institute of Geosciences, Mineralogy and Geochemistry, University of Freiburg, Germany.*

9 *³Institute of Earth and Planetary Sciences, University College London and Birkbeck, University
10 of London, UK.*

11 **corresponding author (email: wanner@geo.unibe.ch, phone: +41316314023, fax:
12 +41316314843)*

13
14 **ABSTRACT**

15 We present Li isotope measurements of groundwater samples collected during drilling of
16 the 57 km long Gotthard rail base tunnel in Switzerland, to explore the use of Li isotope
17 measurements for tracking water-rock interactions in fractured crystalline rocks at temperatures
18 of up to 43°C. The 17 groundwater samples originate from water-conducting fractures within
19 two specific crystalline rock units, which are characterized by a similar rock mineralogy, but
20 significantly different fluid composition. In particular, the aqueous Li concentrations observed in
21 samples from the two units vary from 1-4 mg/L to 0.01-0.02 mg/L. Whereas $\delta^7\text{Li}$ values from the
22 unit with high Li concentrations are basically constant ($\delta^7\text{Li}=8.5\text{-}9.1\text{‰}$), prominent variations are

23 recorded for the samples from the unit with low Li concentrations ($\delta^7\text{Li}=10\text{-}41\text{‰}$). This
24 observation demonstrates that Li isotope fractionation can be highly sensitive to aqueous Li
25 concentrations. Moreover, $\delta^7\text{Li}$ values from the unit with low Li concentrations correlate well
26 with reaction progress parameters such as pH and $[\text{Li}]/[\text{Na}]$ ratios, suggesting that $\delta^7\text{Li}$ values are
27 mainly controlled by the residence time of the fracture groundwater. Consequently, 1D reactive
28 transport modeling was performed to simulate mineral reactions and associated Li isotope
29 fractionation along a water-conducting fracture system using the code TOUGHREACT.
30 Modeling results confirm the residence time hypothesis and demonstrate that the absence of $\delta^7\text{Li}$
31 variation at high Li concentrations can be well explained by limitation of the amount of Li that is
32 incorporated into secondary minerals. Modeling results also suggest that Li uptake by kaolinite
33 forms the key process to cause Li isotope fractionation in the investigated alkaline system
34 ($\text{pH}>9$), and that under slow flow conditions (<10 m/year), this process is associated with a very
35 large Li isotope fractionation factor ($\epsilon \approx -50 \text{‰}$). Moreover, our simulations demonstrate that for
36 simple and well-defined systems with known residence times and low Li concentrations, $\delta^7\text{Li}$
37 values may help to quantify mineral reaction rates if more thermodynamic data about the
38 temperature-dependent incorporation of Li in secondary minerals as well as corresponding
39 fractionation factors become available in the future. In conclusion, $\delta^7\text{Li}$ values may be a
40 powerful tool to track water-rock interaction in fractured crystalline rocks at temperature higher
41 than those at the Earth's surface, although their use is restricted to low Li concentrations and
42 well defined flow systems.

43

44 1. INTRODUCTION

45 The intensity of water-rock interaction in fractured crystalline rocks forms a key parameter
46 in various applications within the field of environmental geochemistry. Examples include
47 enhanced geothermal systems (EGS) where heat extraction mainly depends on accessible
48 fracture surface areas and where water-rock interaction may cause permeability and porosity to
49 decrease over time (Alt-Epping et al., 2013; Stober and Bucher, 2015), nuclear waste repositories
50 to be constructed in crystalline rock environment (e.g., Nordstrom et al., 1989; Molinero et al.,
51 2008; Gimeno et al., 2014) and groundwater contamination affecting fractured crystalline
52 aquifers. The intensity of water-rock interaction in (fractured) crystalline rocks was also
53 proposed to be essential for the global carbon cycle because the interaction of meteoric water
54 with silicate minerals (i.e., chemical weathering) forms an important CO₂ sink (e.g., Berner et al.,
55 1983; Gislason et al., 1996; Francois and Godderis, 1998).

56 Lithium is a trace element that is almost exclusively found in silicate minerals, which
57 makes it a useful tracer for tracking the interaction between water and silicate minerals such as
58 during chemical silicate weathering (Kisakürek et al., 2005; Pogge von Strandmann et al., 2006;
59 Vigier et al., 2009; Millot et al., 2010b; Liu et al., 2015). In particular, tracking Li isotope
60 fractionation is a powerful tool because the two stable Li isotopes (⁶Li, ⁷Li) significantly
61 fractionate during transformation of primary silicate minerals into secondary minerals (Zhang et
62 al., 1998; Pistiner and Henderson, 2003; Vigier et al., 2008; Wimpenny et al., 2010). It is
63 generally agreed that Li isotope fractionation is mainly associated with secondary mineral
64 precipitation whereas Li isotopes dissolve stoichiometrically during (primary) silicate mineral
65 dissolution (Pistiner and Henderson, 2003; Huh et al., 2004). Li isotope fractionation is also
66 promising to track water-rock interaction at temperatures higher than those at the Earth's surface.
67 Vigier et al. (2008) experimentally showed that at a temperature of 250°C the Li isotope

68 enrichment factor for structural Li incorporation into smectite is -1.6‰ and thus greater than the
69 measurement uncertainty for Li isotope measurements. Moreover, Marschall et al. (2007) used a
70 temperature dependent enrichment factor based on a compilation of other studies (Chan et al.,
71 1993; Wunder et al., 2006) to simulate the fate of Li isotopes in subducting slabs suggesting that
72 the Li isotope enrichment factor at 250°C is on the order of -6‰.

73 The numerous studies focusing on chemical silicate weathering at the Earth's surface
74 demonstrate a large range in $\delta^7\text{Li}$ (2-43‰) of dissolved Li, mostly from river waters (e.g., Huh et
75 al., 1998; Kisakürek et al., 2005; Pogge von Strandmann et al., 2006; Millot et al., 2010b;
76 Dellinger et al., 2015; Liu et al., 2015). Whereas the literature agrees that increasing the ratio of
77 Li uptake by secondary minerals to Li release from primary mineral dissolution drives $\delta^7\text{Li}$ to
78 higher values, it is still under debate if and how temporal and spatial $\delta^7\text{Li}$ distributions can be
79 used as a proxy for geomorphic and/or climatic variations. In particular, the increasing seawater
80 $\delta^7\text{Li}$ values observed over the last ca. 56 Ma (Misra and Froelich, 2012) have been attributed
81 either to increasing tectonic activities (Misra and Froelich, 2012; Li and West, 2014; Wanner et
82 al., 2014) or to a decreasing soil production rate and thus to cooler climatic conditions (Vigier
83 and Godd ris, 2015). In contrast to surface water samples, $\delta^7\text{Li}$ in water from hydro-geothermal
84 sites with temperatures of up to 335°C varies only in a narrow range of 0-11‰ (Chan et al.,
85 1993; Chan et al., 1994; Millot and Negrel, 2007; Millot et al., 2010a; Henchiri et al., 2014;
86 Sanjuan et al., 2014; Pogge von Strandmann et al., 2016). Despite this relatively narrow range, it
87 was proposed that for such systems $\delta^7\text{Li}$ may operate as a geothermometer to estimate the
88 corresponding reservoir temperature. Also it was proposed to use $\delta^7\text{Li}$ from hydro-geothermal
89 sites as proxy for the origin of the hydrothermal fluid, and/or as proxy for the intensity of water-
90 rock interaction (Millot and N grel, 2007; Millot et al., 2010a).

91 In this study, we present Li isotope measurements of groundwater collected during the
92 construction of the 57 km long Gotthard rail base tunnel in Switzerland. Major anion and cation
93 concentrations have been reported by Seelig and Bucher (2010) and Bucher et al. (2012). Our
94 groundwater samples originate from water-conducting fractures within two specific crystalline
95 rock units and show on-site temperatures of up to 43°C. The hydrogeochemical conditions are
96 thus similar to those at future EGS sites although the temperature is significantly lower than the
97 target EGS temperature of 180°C or greater. The main objective was to explore the use of Li
98 isotope measurements to track water–rock interaction in an EGS-like system with temperatures
99 higher than those at the Earth’s surface. Furthermore, an essential part of our study was to
100 simulate Li isotope fractionation occurring in a fractured crystalline aquifer using the reactive
101 transport modeling code TOUGHREACT V3 (Xu et al., 2014). In this context, TOUGHREACT
102 was updated to allow defining a maximum amount of Li that can be incorporated into secondary
103 minerals.

104

105 **2. SITE DESCRIPTION AND SAMPLING**

106 The new 57 km long Gotthard rail base tunnel in Switzerland is the longest and deepest
107 tunnel in the world. The tunnel crosses the Alps at a base level of ca. 500 m a.s.l. and its
108 construction was divided into five sections, which were excavated separately by drilling vertical
109 access shafts. Our study relates to the Amsteg section in the northern part of the tunnel (Fig 1).
110 This 11.5 km long section was constructed between 2003 and 2006 using a 400 m long tunnel-
111 boring machine (TBM). The section exclusively penetrates crystalline basement rocks of the Aar
112 massif, which is a NE-SW trending complex of Variscan basement overprinted by Alpine
113 metamorphism and deformation (Abrecht, 1994; Schaltegger, 1994; Labhart, 1999). The units

114 intersected along the Amsteg section show a similar mineralogical composition with dominating
115 quartz, albite, K-feldspar and chlorite and minor amounts of biotite and muscovite as well as
116 secondary calcite and accessory pyrite (Bucher et al., 2012). The thickness of the rock column
117 above the tunnel is up to 2200 m (Fig. 1). According to Bucher et al. (2012), the chemical
118 composition of groundwater samples at tunnel level is dominated by the infiltration of meteoric
119 water at the surface and subsequent reaction with the fractured crystalline rocks during transport
120 to the tunnel level. This infiltration model agrees with steeply dipping rock units (Fig. 1) and the
121 presence of a predominant, nearly vertical fracture system. Preliminary $\delta^2\text{H}$ and $\delta^{18}\text{O}$
122 measurements indicate a dominating meteoric origin of groundwater collected. More information
123 regarding the geology and hydrology of the Amsteg section is provided by Bucher and al. (2012)
124 and references therein.

125 A total of 122 groundwater samples were collected from water conducting fractures.
126 Groundwater samples were collected from natural inflows along fractures after these were cut by
127 the TBM and before they were sealed with concrete. Due to the induced pressure drop, the water
128 was flowing from the fractures with discharge rates between 3×10^{-4} L/s and 6 L/s. Based on
129 differences in dissolved Li concentrations, 17 groundwater samples from two distinct geological
130 units within the Amsteg section, the Bristner Granite and the migmatitic unit called BuMigIII
131 (Fig. 1) were selected for the analyses of Li and Li isotopes. In addition, Li concentrations were
132 determined on rock samples of the two units that were retrieved from cored test drillings
133 performed in front of the TBM. At similar average water influx into the tunnel (Bucher et al.,
134 2012), groundwater draining the Bristner Granite shows Li concentration between 1-4 mg/L and
135 much lower concentrations of 0.01-0.02 mg/L in the BuMigIII.

136

137 **3. METHODS**

138

139 **3.1. Li concentration measurements**

140

141 *3.1.1. Solid Li*

142 Bulk rock Li concentrations were measured by atomic adsorption spectroscopy using a
143 Vario 6 spectrometer from Analytic Jena at the University of Freiburg, Germany. To do so, cores
144 retrieved from test drillings into the Bristner Granite and into BuMigIII were milled to a fine
145 powder. For each sample, 0.1 g was digested in 5 mL 65% HNO₃ and 1 mL 33% H₂O₂. To
146 ensure that the entire sample was digested, samples were exposed to 160°C for 6 minutes and to
147 215°C for 25 minutes using a MLS microwave. The analytical uncertainty was ±5%.

148 Selected trace element concentrations including Li of individual mineral phases and phase
149 mixtures within the Bristner Granite and BuMigIII were measured by Laser ablation ICP-MS at
150 the University of Bern, Switzerland, on polished thin sections (50 µm). The system at the
151 University of Bern consists of a Geolas Pro 193 nm ArF Excimer laser (Lambda Physik,
152 Germany) coupled with an ELAN DRCE quadrupole mass spectrometer (QMS; Perkin Elmer,
153 USA). Details on the setup and optimization strategies are given in Pettke et al. (2012). Daily
154 optimization of the analytical conditions were performed to satisfy a ThO production rate of <0.2
155 % (i.e., Th/ThO intensity ratio < 0.002) and to achieve robust plasma conditions monitored by a
156 Th/U sensitivity ratio of 1 as determined on the SRM610 glass standard. External standardization
157 was performed employing SRM610 from NIST with preferred values reported in Spandler et al.
158 (2011), and bracketing standardization provided a linear drift correction. Internal standardization
159 was done by summing the major element oxides to 100 wt% or 98-97 wt% for biotite and

160 hydrous mineral mixtures (containing muscovite, biotite, minor chlorite and Fe_2O_3). Data were
161 reduced using SILLS (Guillong et al., 2008), with limits of detection calculated for each element
162 in every analysis following the formulation detailed in Pettke et al. (2012).

163

164 *3.1.2. Dissolved Li*

165 Li concentrations available from the previous study (Bucher et al., 2012) were determined
166 using a DX-120 ion chromatograph (IC), with a detection limit of 0.01 mg/L and an analytical
167 uncertainty of 0.005 mg/L for concentrations below 0.1 mg/L. Because groundwater samples
168 originating from BuMigIII displayed Li concentrations on the order of the detection limit (0.01-
169 0.02 mg/L), Li concentration measurements were repeated for these samples using an Analytic
170 Jena ContrAA 700 BU atomic adsorption spectrometer in the graphite furnace mode (GFAAS) at
171 the University of Bern. Standardization was performed using the Merck 4 Certipur standard and
172 tested with the Sigma 6 and Merck 4 Li single element standards. Within the standardization
173 range of 1.25–5 $\mu\text{g/L}$, the Li recovery was >90% yielding an analytical uncertainty of $\pm 10\%$.
174 Reported Li concentrations are average values of triplicate analyses.

175

176 **3.2. Li isotope measurements**

177 Lithium isotope measurements of groundwater samples were performed as detailed in
178 Pogge von Strandmann and Henderson (2015) and Pogge von Strandmann et al. (2011). Briefly,
179 this entailed running approximately 20 ng of Li through a two-step cation exchange column
180 method, containing AG50W X-12 resin, and using dilute HCl as an eluent.

181 Samples were then analysed on a Nu Instruments HR MC-ICP-MS at Oxford University,
182 by sample-standard bracketing with the standard L-SVEC. Individual analyses consisted of three

183 separate repeats of 10 ratios (10 s integration time per ratio), giving a total integration time of
184 300 s/sample during each analytical session. At an uptake rate of 75 $\mu\text{l}/\text{min}$, the sensitivity for a
185 20 ng/ml solution is ~ 18 pA of ${}^7\text{Li}$ using 10^{11} Ω resistors. Background instrumental Li intensity,
186 typically ~ 0.01 pA, was subtracted from each measurement. Li isotope measurements are
187 reported as ${}^7\text{Li}/{}^6\text{Li}$ ratio in terms of the δ -notation relative to the Li isotope standard L-SVEC
188 ($\delta^7\text{Li} = 0.0\text{‰}$) and are given in ‰:

189

$$190 \quad \delta^7\text{Li} = \left[\left(\frac{{}^7\text{Li}/{}^6\text{Li}_{\text{sample}}}{{}^7\text{Li}/{}^6\text{Li}_{\text{L-SVEC}}} \right) - 1 \right] \cdot 1000 \quad (1)$$

191

192 To assess accuracy and precision, both seawater and the international USGS standard BCR-2
193 were analysed. Both standards analysed with these samples (seawater: $\delta^7\text{Li} = 31.5 \pm 0.4\text{‰}$; BCR-
194 2: $2.7 \pm 0.3\text{‰}$) agree well with their long-term averages (seawater: $31.2 \pm 0.6\text{‰}$, $n=46$; BCR-2:
195 $2.6 \pm 0.3\text{‰}$, $n=17$; Pogge von Strandmann et al., 2011, Pogge von Strandmann and Henderson,
196 2015). The total procedural blank for Li isotopes is effectively undetectable (<0.005 ng Li).

197

198 **3.3. Reactive transport modeling**

199 A series of 1D reactive transport simulations using TOUGHREACT V3 (Xu et al., 2014)
200 was performed to simulate the interaction of infiltrating meteoric water with granitic rock and its
201 specific effects on aqueous $\delta^7\text{Li}$. TOUGHREACT has been previously applied to evaluate
202 isotopic fractionation coupled to water-rock interaction and hydrological processes in a variety of
203 subsurface environments and laboratory experiments (Sonnenthal et al., 1998; Singleton et al.,
204 2005; Wanner and Sonnenthal, 2013). Specifically, it has been used to simulate Li isotope
205 fractionation in granitic as well as basaltic systems (Wanner et al., 2014; Liu et al., 2015).

206 Furthermore, the TOUGHREACT approach for simulating isotopic fractionation coupled to
 207 mineral precipitation has been recently benchmarked (Wanner et al., 2015).

208

209 3.3.1. Model formulation

210

211 Mineral dissolution and precipitation

212 TOUGHREACT V3 (Xu et al., 2014) computes mineral dissolution and precipitation
 213 reactions (mol/s/kg_{H2O}) as kinetic reactions based on transition state theory (TST) (Lasaga,
 214 1984):

$$215 \quad r = A_r \cdot k \cdot \left[1 - \left(\frac{Q}{K} \right)^m \right]^n = A_{rfrac} \cdot k \cdot \left[1 - \left(\frac{Q}{K} \right)^m \right]^n \quad (2)$$

216

217 where A_r refers to the mineral reactive surface area (m²/kg_{H2O}). In case of fracture flow, A_r is
 218 assumed to be the same for each mineral (Xu et al., 2014) and corresponds to the reactive surface
 219 area of the simulated vertical fracture system A_{rfrac} . Q and K refer to the ion activity product and
 220 equilibrium constant of a mineral dissolution/precipitation reaction, respectively. Exponents m
 221 and n are fitting parameters that must be experimentally determined. However, for or this study,
 222 they were taken to be unity. The temperature and pH dependent rate constant k is formulated as:

223

$$224 \quad k = k_{25}^n \exp \left[\frac{-E_a^n}{R} \left(\frac{1}{T} - \frac{1}{298.15} \right) \right] + k_{25}^{ac} \exp \left[\frac{-E_a^{ac}}{R} \left(\frac{1}{T} - \frac{1}{298.15} \right) \right] a_{H^+}^{m_{ac}} + k_{25}^{ba} \exp \left[\frac{-E_a^{ba}}{R} \left(\frac{1}{T} - \frac{1}{298.15} \right) \right] a_{H^+}^{m_{ba}}$$

225 (3)

226 where k_{25} refers to reaction rate constants at 25°C (mol/m²/s), E_a is the activation energy (kJ/mol)
227 and T and R are the temperature (K) and ideal gas constant, respectively. The superscripts n , ac
228 and ba denote neutral, acidic and basic conditions, respectively, a_{H^+} refers to the H⁺ activity, and
229 m_{ac} and m_{ba} refer to the reaction order with respect to H⁺ (i.e., pH) at acidic and basic conditions,
230 respectively. In order to calculate effective precipitation and dissolution rates (eqs. 2,3), reaction
231 rate constants were defined according to the compilation of Palandri and Kharaka (2004)
232 whereas equilibrium constants were taken from the Soltherm.H06 database (Reed and Palandri,
233 2006). Mineral stoichiometries, thermodynamic and kinetic parameters of minerals considered
234 for our simulations are summarized in Table 1.

235

236 *Simulation of Li isotope fractionation*

237 The fate of individual Li isotopes was simulated according to the approach recently
238 presented by Wanner et al. (2014). To do so, ⁶Li and ⁷Li were defined as primary aqueous
239 species and were incorporated into the mineral stoichiometry of Li-bearing minerals. Similar to
240 the model of Bouchez et al. (2013), our approach does not distinguish between Li exchange-, Li
241 surface complexation or Li incorporation into a crystal. Accordingly, Li isotope fractionation is
242 solely simulated during Li incorporation of dissolved Li into precipitating minerals. Besides the
243 lack of fractionation factors distinguishing between Li incorporation, Li exchange and sorption,
244 the low exchange capacity of crystalline rocks (Mazurek et al., 2003) is supportive to such
245 assumption. Incorporation of Li in secondary clay minerals is limited and occurs only at trace
246 concentrations in the ppm range (e.g., Tardy et al., 1972). The concentration differences by
247 orders of magnitudes between major and trace elements in such secondary minerals may pose
248 convergence problems due to the large differences in exponents in the ion-activity product

249 included in the rate law (eq. 2). To circumvent this problem, precipitation of Li-bearing
 250 secondary minerals was simulated defining a solid solution with three different endmembers (see
 251 Wanner et al., 2014): (i) a pure, non Li-bearing secondary mineral endmember, (ii) a pure ⁶Li
 252 endmember and (iii) a pure ⁷Li endmember. The pure ⁶Li and ⁷Li endmembers are hypothetical,
 253 but their specification solves the above mentioned numerical problems, and their log(K) values
 254 are obtained by fitting to the observed aqueous Li concentration and the amounts of Li analyzed
 255 in secondary minerals. The precipitation rate r_{prec} of the solid solution of Li-bearing secondary
 256 minerals is then calculated as the sum of the individual endmember precipitation rates r_{2ndmin}
 257 (pure secondary mineral), r_{6Li} and r_{7Li} :

$$259 \quad r_{prec} = r_{2ndmin} + r_{6Li} + r_{7Li} \quad (4)$$

261 The rate of a specific endmember, r_{endm} , is calculated according to a TST-like expression:

$$263 \quad r_{endm} = A \cdot k \cdot \left(1 - \frac{Q_{endm}}{K_{endm}} \right) + k \cdot A \cdot (x_{endm} - 1) \quad (5)$$

264 where x_{endm} refers to the mole fraction of a specific secondary mineral endmember. For the
 265 hypothetical, pure ⁶Li and ⁷Li endmembers x_{6Li} and x_{7Li} are calculated according to:

$$268 \quad x_{6Li} = \frac{(Q_{6Li} / K_{6Li})}{(Q_{6Li} / K_{6Li}) + (Q_{7Li} / K_{7Li}) + (Q_{2ndmin} / K_{2ndmin})} \quad (6)$$

$$x_{7Li} = \frac{(Q_{7Li} / K_{7Li})}{(Q_{6Li} / K_{6Li}) + (Q_{7Li} / K_{7Li}) + (Q_{2nd\ min} / K_{2nd\ min})} \quad (7)$$

270

271 Equations (6) and (7) ensure that the amount of Li that is incorporated into a secondary
 272 mineral reflects the Li concentration of the aqueous solution. Accordingly, the amount of Li
 273 removed by precipitation increases with increasing aqueous Li concentration. By doing so, our
 274 model is in agreement with an experimental study showing that Li concentrations of synthesized
 275 smectites are correlated with corresponding aqueous Li concentrations (Decarreau et al., 2012).
 276 Decarreau et al. (2012), however, also showed that the total amount of Li that can be
 277 incorporated is limited due to structural reasons. We therefore updated TOUGHREACT so that
 278 the user now has the option to specify the maximum amount of Li that is allowed to precipitate in
 279 a given solid solution. To do so, the user needs to define the maximum Li mol fraction $x_{maxLi} =$
 280 $x_{6Li} + x_{7Li}$ that corresponds to a particular maximum Li content (e.g., in $\mu\text{g/g}$) in a specific mineral
 281 solid solution phase. For the pure (hypothetical) ^6Li and ^7Li endmembers, the maximum mol
 282 fraction then become:

283

$$x_{6Li_max} = x_{maxLi} \frac{(Q_{6Li} / K_{6Li})}{(Q_{6Li} / K_{6Li}) + (Q_{7Li} / K_{7Li})} \quad (8)$$

$$x_{7Li_max} = x_{maxLi} \frac{(Q_{7Li} / K_{7Li})}{(Q_{6Li} / K_{6Li}) + (Q_{7Li} / K_{7Li})} \quad (9)$$

286

287 Subsequently, x_{6Li_max} and x_{7Li_max} are compared with x_{6Li} and x_{7Li} as calculated by equations (6) or
 288 (7). If $x_{6Li} > x_{6Li_max}$ and $x_{7Li} > x_{7Li_max}$ the precipitation rate of the pure 6Li and 7Li endmembers are
 289 no longer calculated according to equation (5) and become:

290

$$291 \quad r_{6Li} = r_{pure2nd} \cdot x_{6Li_max} \quad (10)$$

$$292 \quad r_{7Li} = r_{pure2nd} \cdot x_{7Li_max} \quad (11)$$

293

294 Using the solid solution approach described above allows defining an experimentally determined
 295 or otherwise inferred isotope fractionation factor α and corresponding enrichment factor ε
 296 associated with mineral precipitation for a particular simulation run:

297

$$298 \quad \alpha = \frac{K_{6Li}}{K_{7Li}} \quad (12)$$

299

$$300 \quad \varepsilon = (\alpha - 1) \cdot 1000 \approx \Delta^7Li = \delta^7Li_{2ndMin} - \delta^7Li_{solution} \quad (13)$$

301

302 It should be noted that our approach for simulating Li isotope fractionation is different
 303 from other approaches (Lemarchand et al., 2010; Bouchez et al., 2013; Pogge von Strandmann et
 304 al., 2014). Instead of exclusively focusing on the Li system, we use a fully-coupled reactive
 305 transport modeling code (see Steefel et al., 2015 for a summary of available codes). In doing so,
 306 our approach may simulate the chemical evolution of an entire porous media and parameters
 307 other than aqueous Li concentrations and δ^7Li values can be used to constrain the model as well.

308

309 **4. RESULTS**

310

311 **4.1. Solid [Li] measurements**

312 Li concentration data of primary minerals and mineral mixtures from the Bristner Granite
313 and the migmatitic unit BuMigIII are summarized in Table 2. The full chemical analysis of each
314 laser ablation ICP-MS measurement is listed in the electronic appendix. Bulk rock Li
315 concentrations average at 6 for the Bristner Granite and 9 $\mu\text{g/g}$ for BuMigIII. In both units,
316 elevated average Li concentrations of 463 (Bristner Granite) and 217 $\mu\text{g/g}$ (BuMigIII) were
317 observed in sheet silicates such as chloritized biotite and muscovite. Further differences between
318 the two units include higher Li concentrations in K-feldspar (45 $\mu\text{g/g}$) of the BuMigIII compared
319 to those in K-feldspar (2.4 $\mu\text{g/g}$) of the Bristner Granite (Table 2).

320

321 **4.2. Aqueous Li concentrations and $\delta^7\text{Li}$ values**

322 Concentrations and $\delta^7\text{Li}$ values of aqueous Li of 17 groundwater samples originating from
323 the Bristner Granite and BuMigIII are presented in Table 3 in conjunction with field parameters
324 and major cations and anions concentrations reported in Bucher et al. (2012). Computed
325 saturation indices of selected primary and secondary minerals are listed in Table 4. Groundwater
326 temperature correlates with the thickness of the rock column above the tunnel. In the Bristner
327 Granite, groundwater discharges at temperatures from 21.5 to 25.1°C at a corresponding rock
328 overburden of <500 m. In the BuMigIII groundwater, temperature is remarkably constant (42.6-
329 43.7°C) at a corresponding overburden of ca. 2000 m, except for sample A103 (36.7°C), which
330 also displays differences in the chemical composition (e.g., Ca, Mg, pH). Groundwater sample
331 A126 displays strongly elevated SO_4 and Ca concentrations compared to the majority of

332 BuMigIII groundwater (Table 3). In accordance with the anhydrite saturation index close to zero
333 (Table 4), this was attributed to anhydrite dissolution during flow along anhydrite-bearing
334 fractures (Bucher et al., 2012). Aqueous Li concentrations vary between 1.6 and 3.2 mg/L in
335 groundwater from the Bristner Granite compared to 0.010 and 0.017 mg/L in groundwater from
336 the BuMigIII. The orders of magnitude difference in Li concentration is striking given the
337 similarity of the bulk rock Li concentrations, which differ only by a factor of about 1.5 (Table 2).

338 Similar to aqueous Li concentrations, $\delta^7\text{Li}$ values of groundwater from the two units show
339 a distinct behavior. The high-Li groundwaters of the Bristner Granite show very little variation in
340 their $\delta^7\text{Li}$ values (8.5-9.1‰). In contrast, the low-Li groundwaters from BuMigIII show a very
341 strong variation (10-41‰). These latter groundwaters display a positive correlation between $\delta^7\text{Li}$
342 values and pH but a negative correlation between $\delta^7\text{Li}$ and aqueous Li concentrations and the
343 molar Li/Na ratio, except for the exceptional groundwater samples A103 and A126, as discussed
344 above (Fig. 2a-c). Moreover, $\delta^7\text{Li}$ and Li seem to follow a Rayleigh-type fractionation model
345 with $\alpha = 0.95$ ($\epsilon = -50\text{‰}$) (Fig. 2d), suggesting a single process being responsible for the
346 observed variation in $\delta^7\text{Li}$ values.

347

348 **5. DISCUSSION**

349

350 **5.1. Source of aqueous Li**

351 Seelig and Bucher (2010) demonstrated that Cl is a passive tracer in groundwater of the
352 Amsteg section of the Gotthard rail base tunnel and suggested that Cl is derived from porewaters
353 trapped in the matrix of the crystalline rocks. Further, they proposed that the trapped porewater
354 represents the remnants of a hydrothermal fluid that evolved during alpine metamorphism.

355 Interestingly, in the Bristner Granite groundwater, Li concentrations correlate well with Cl
356 concentrations ($r^2=0.95$, Fig. 3) inferring that Li is likely derived from the same porewater source
357 as Cl. This observation is important because it demonstrates that meteoric water infiltrating into
358 a crystalline basement may pick up Li from sources other than from interaction with rock
359 forming minerals.

360 In contrast to the Bristner Granite groundwater, Cl and Li concentrations in BuMigIII
361 groundwater are orders of magnitude lower and no clear correlation is observed (Table 3). The
362 molar Cl/Li ratio, however, is of the same order of magnitude as recorded for the Bristner
363 Granite water samples (10-30). This observation suggests that a porewater of a similar
364 composition may form a major Li source for BuMigIII groundwater as well. Alternative Li
365 sources are the dissolution of Li-bearing minerals or mixing of the infiltrating meteoric water
366 with an external groundwater (i.e, originating from another lithology) characterized by an
367 elevated Li concentration and a similar Li/Cl ratio as observed in the Bristner Granite
368 groundwater.

369

370 **5.2. Secondary minerals**

371 Lithium uptake by precipitation of Fe- and Al-bearing secondary mineral or adsorption of
372 Li to these minerals have been proposed to form the major process for Li isotope fractionation
373 observed in the shallow subsurface (Zhang et al., 1998; Pistiner and Henderson, 2003; Vigier et
374 al., 2008; Wimpenny et al., 2010). Based on computed saturation indices (Table 4), kaolinite is
375 the only secondary Al-bearing secondary phase that is potentially precipitating from the
376 BuMigIII groundwater under the given condition ($SI>0$), whereas the Bristner Granite
377 groundwater is supersaturated with respect to gibbsite and illite as well. To assess the

378 precipitation of kaolinite from BuMigIII groundwater, it has to be acknowledged that the
379 equilibrium constant of kaolinite is associated with a large uncertainty (Trotignon et al., 1999),
380 which is reflected by its changing saturation state in BuMigIII groundwater when using different
381 thermodynamic databases (Table 4). The range of $\log(K)$ values for kaolinite tabulated in
382 different thermodynamic databases is at least partly related to differences in solubility
383 experiments (e.g. acid vs alkaline conditions, temperature), but also to analytical difficulties (e.g.
384 Al and Si colloids). Figure 4 shows the relation of the kaolinite equilibrium constant tabulated in
385 the Soltherm.H06 (Reed and Palandri, 2006) and EQ3/6 database (Wolery, 1992). Temperature
386 dependent $\log(K)$ tabulated in the Soltherm.H06 database reproduces well $\log(K)$ values derived
387 from kaolinite solubility experiments performed at temperatures of 60, 90 and 110°C and at
388 similar pH values, as observed in our system (up to pH 9) (Devidal et al., 1996). In contrast,
389 temperature dependent $\log(K)$ values derived from the EQ3/6 database (Wolery, 1992)
390 overestimate the Devidal et al. (1996) values. However, they are within the range of kaolinite
391 solubilities determined for temperatures between 22-25°C (Polzer and Hem, 1965; Kittrick,
392 1966; Reesman and Keller, 1968; May et al., 1986; Yang and Steefel, 2008) and the solubility
393 experiment performed by Nagy et al., (1991) at 80°C and pH 3. Overall, computed saturation
394 indices (Table 4) and thermodynamic considerations (Fig. 4) support the use of the
395 Soltherm.H06 database and suggest that kaolinite is the dominating secondary Al phase
396 precipitating from the BuMigIII groundwater. The restricted access to water-conducting
397 fractures, however, did not allow confirmation of the presence of kaolinite although it has been
398 observed as low-T alteration product in various crystalline rock environments (e.g., Grimaud et
399 al., 1990; Michard et al., 1996; Gimeno et al., 2014).

400 Our groundwater samples display dissolved oxygen concentrations below detection limit
401 demonstrating that reducing conditions are established. Under reducing conditions, the formation
402 of Fe(III)-oxides such as goethite, ferrihydrite, lepidocrocite, and hematite is absent
403 (Schwertmann, 1988). Accordingly, their formation and corresponding sorption reactions are
404 restricted to the domain very close to the surface where the dissolved oxygen concentration in
405 infiltrating meteoric water is in equilibrium with atmospheric oxygen. The limited formation of
406 Fe-bearing secondary minerals infers that Li isotope fractionation is primarily caused by Li
407 uptake by kaolinite (BuMigIII) or other Al-bearing secondary minerals (Bristner Granite).

408

409 **5.3. Diffusive Li isotope fractionation and anthropogenic Li contamination**

410 If Li influx into the fracture groundwater were occurring entirely by diffusion from a
411 porewater Li source, diffusive fractionation is a likely process to cause a $\delta^7\text{Li}$ variation in
412 addition to Li uptake by secondary minerals (Richter et al., 2006; Bourg and Sposito, 2007).
413 Owing to the difference in mass, the diffusion coefficient of ^6Li is larger than that for ^7Li leading
414 to enrichment in ^6Li (low $\delta^7\text{Li}$) in the groundwater. Accordingly, diffusive Li isotope
415 fractionation would partially mask the $\delta^7\text{Li}$ increase inherited from Li isotope fractionation
416 associated with secondary mineral precipitation. Indeed, it would yield an even higher intrinsic
417 fractionation factor than the -50‰ obtained from the Rayleigh-type model (Fig. 2d).

418 In contrast to diffusive Li isotope fractionation, anthropogenic contamination of Li can be
419 excluded based on the infiltration area in remote high-alpine area and the high hydraulic pressure
420 of about 100 bar at the discharge locations (Masset and Loew, 2013). Also, if any artifacts
421 occurred during sampling, major species concentrations were affected as well and their

422 concentrations could not be approximated by solely simulating water-rock interaction between
423 meteoric water and pristine granite such as shown below.

424

425 **5.4. Hypothesis for observed $\delta^7\text{Li}$ variation**

426 The most striking observation from our measurements is that significant $\delta^7\text{Li}$ variation only
427 occurs at low Li concentrations, suggesting that the variation is highly sensitive to the aqueous Li
428 concentration. The second key observation is the negative correlation between $\delta^7\text{Li}$ and the Li
429 concentration as well as the positive correlation between $\delta^7\text{Li}$ and pH seen in the BuMigIII
430 groundwater (Fig. 2a,b). Our approach is to first explore the process(es) controlling the Li
431 system in a single hydrogeochemical system such as the BuMigIII groundwater, before
432 comparing the different settings (BuMigIII vs. Bristner Granite).

433 The BuMigIII groundwaters likely have different residence times within the rock column
434 above the tunnel due to a variation in fracture permeability and connectivity. Variable residence
435 times are consistent with the 2 orders of magnitude variation in flow rates (Table 3) and the
436 observed trends in chemical and Li-isotope composition (Fig. 2a,c). In granitic systems, the pH
437 increases with reaction progress (Nordstrom et al., 1989; Grimaud et al., 1990; Bucher et al.,
438 2012; Gimeno et al., 2014) and the Li/Na ratio may form an excellent proxy for the degree of
439 water-rock interaction (e.g., residence time, reaction progress) that inversely correlates with $\delta^7\text{Li}$
440 (Liu et al., 2015). The Li/Na ratio is indicative because Na concentrations are several orders of
441 magnitude greater than Li concentrations, and thus not as strongly affected by minor uptake by
442 secondary mineral precipitation (e.g., kaolinite). In case of a discrete Li influx such as from an
443 external groundwater source (Fig. 5b), Na release from primary minerals is ongoing, which also
444 yields a decrease of the Li/Na ratio with flow distance and reaction progress.

445 Higher residence time of groundwater results in increased water-rock interaction and thus
446 increased precipitation of Li-bearing kaolinite, which drives $\delta^7\text{Li}$ to higher values (Wanner et al.,
447 2014). Observing a negative correlation between $\delta^7\text{Li}$ and the Li concentration must thus be
448 inherited from the spatial release rate of the actual Li source along the infiltration path in relation
449 to the corresponding Li uptake rate by secondary minerals. The amount of data to quantitatively
450 assess the role of the potential Li sources (Li-bearing minerals, porewater, external
451 groundwater), however, are limited. Therefore and in terms of a sensitivity analyses, a series of
452 reactive transport model simulations were performed by varying the Li source as well as the
453 parameters controlling the Li system in order to unravel how these parameters affect aqueous
454 $\delta^7\text{Li}$ values and Li concentrations in the BuMigIII groundwater.

455

456 **6. REACTIVE TRANSPORT MODELING**

457

458 **6.1. Model setup**

459 Reactive transport model simulations were performed for a simplified vertical, fully-
460 saturated 2000 m long 1D flow path consisting of 1000 grid blocks of 2 m length (Fig. 5). A
461 fixed linear temperature gradient of 10 to 43°C was specified from the upstream to the
462 downstream model boundary. With these specifications, the model represents the geometry
463 where the tunnel intersects with BuMigIII. In contrast to other studies (DePaolo, 2006; Waber et
464 al., 2012; Brown et al., 2013), our model does not explicitly consider diffusion between water
465 flowing along fractures and porewater residing in the intact rock matrix. In doing so, we
466 exclusively simulate reactive transport along one particular fracture system. The porosity and
467 permeability relevant for fluid flow in fractured crystalline rocks depend on the fracture spacing

468 and aperture (Caine and Tomusiak, 2003; MacQuarrie and Mayer, 2005; Sonnenthal et al.,
469 2005). None of these parameters are explicitly known for the present system so that individual
470 simulations were run at a constant flow rate using a fixed fracture porosity of 1% (Fig. 5). To
471 account for the unknown residence time within the rock column above the tunnel, simulations
472 were run for flow velocities ranging from 0.2 to 20 m/year, which approximately reflect the
473 variation of flow rates observed for the BuMigIII samples (0.01-2.5 L/s). The specified velocity
474 range also covers the range in hydraulic conductivity ($3-7 \times 10^{-8}$ m/s) reported for fracture zones
475 along the nearby Sedrun section of the tunnel (Masset and Loew, 2013).

476

477 **6.2. Initial and boundary conditions**

478 Water in equilibrium with atmospheric CO₂ and O₂ was specified as initial and upper
479 boundary condition to simulate the infiltration of meteoric water into the BuMigIII rock column
480 above the tunnel (Table 5). The solid part of the model domain is given by the granitic
481 composition of the BuMigIII rock (Table 5). Plagioclase has only a minor anorthite component
482 and pure albite was used in the calculations. In contrast, biotite and chlorite were defined as solid
483 solutions between the corresponding Fe (annite and chamosite) and Mg endmembers (phlogopite
484 and clinocllore) according to the analyzed Mg/Fe ratios (el. appendix).

485

486 *6.2.1. Li source and secondary minerals*

487 Li was introduced by defining two different Li sources: (i) Li-bearing biotite with a Li
488 concentration of 217 µg/g as measured in chloritized biotite of the BuMigIII rock (Table 2) and
489 (ii) a hypothetical Li_{0.04}Na_{0.96}Cl solid phase that acts either as a proxy for matrix porewater or an
490 external, ad-mixed groundwater Li source. The Cl/Li ratio of 25 defined for this hypothetical

491 phase corresponds to the ratio obtained from the linear correlation between Cl and Li observed
492 for Bristner Granite groundwater (Fig. 3), while charge balance was maintained by including Na.
493 An initial $\delta^7\text{Li}$ value of 1.7‰ was assigned to Li-bearing biotite, corresponding to the average
494 $\delta^7\text{Li}$ value determined for a large series of different granites (Teng et al., 2009). In contrast, the
495 average Bristner Granite groundwater $\delta^7\text{Li}$ value of 8.7‰ (Table 3) was assigned to the
496 hypothetical $\text{Li}_{0.04}\text{Na}_{0.96}\text{Cl}$ solid phase based on our concept that Li in the BuMigIII is derived
497 from a similar source as in the Bristner Granite.

498 While all simulations considered the Li-bearing biotite source, two scenarios were run for
499 the $\text{Li}_{0.04}\text{Na}_{0.96}\text{Cl}$ source. The first scenario considered a constant zero order dissolution rate of
500 2×10^{-15} mol/kg_{H₂O}/s occurring along the entire model domain and corresponding to a Li influx
501 from a porewater source (continuous Li influx scenario, Fig. 5a). This yields a Li concentration
502 of 0.017 mg/L at the tunnel level what corresponds to the maximum concentration observed in
503 BuMigIII groundwater samples (Fig. 2). The second set considered a single point Li influx after
504 an arbitrary flow distance of 400 m and simulates a situation where Li in the BuMigIII
505 groundwater is ad-mixed by an external fracture groundwater to the infiltrating meteoric water
506 (mixing scenario, Fig. 5b). To do so, the Li concentration of the simulated groundwater mixture
507 was set to 0.017 mg/L at $z = -400\text{m}$.

508 Kaolinite is the only secondary Al-phase precipitating in our model and Li uptake by
509 kaolinite is the only process to cause Li isotope fractionation. Based on the observation that the
510 SiO_2 concentrations of the 122 tunnel waters are solubility-controlled by quartz above a pH of
511 ca. 9 (Bucher et al., 2012), secondary quartz was allowed to precipitate as well. The same applies
512 for goethite.

513

514 6.2.2. Sensitivity analyses

515 Our approach for simulating Li isotope fractionation allows defining a Li isotope
516 fractionation factor as well as a maximum amount of Li that can be incorporated in secondary
517 minerals. Since both parameters are unknown, simulations were run for Li isotope enrichment
518 factors of -25, -37.5 and -50‰ associated with Li uptake by kaolinite and for maximum Li
519 concentrations in kaolinite of 25, 50 and 75 µg/g to test their impact on the model results.
520 Whereas these maximum Li concentrations cover the Li concentration range observed in natural
521 kaolinite (Tardy et al., 1972; Vigier and Godd eris, 2015), Li isotope enrichment factors of -37.5
522 and -50‰ are outside the range inferred so far for secondary mineral precipitation (\approx -10 to -
523 30‰) (Zhang et al., 1998; Huh et al., 2001; Pistiner and Henderson, 2003; Kisk erek et al.,
524 2005; Pogge von Strandmann et al., 2006; Vigier et al., 2008; Pogge von Strandmann et al.,
525 2010). The range in ϵ was expanded to higher values because the Li concentration and isotope
526 data from BuMigIII groundwater revealed an ϵ -value of -50‰ when applying a Rayleigh-type
527 model (Fig. 2d). A temperature effect on epsilon such as observed for hydro-geothermal system
528 (Marschall et al., 2007; Vigier et al., 2008; Verney-Carron et al., 2015; Pogge von Strandmann et
529 al., 2016) was not considered because within the temperature range of our model (10-43°C), it is
530 likely smaller than the uncertainty of ϵ -values reported for Li uptake by secondary minerals as
531 well as the ϵ -range considered in the sensitivity analyses. Additional sensitivity simulations
532 included a reduction of the kaolinite precipitation rate constant by 67% and 33% of the initially
533 chosen value (base case, Table 1), a variation of the $\delta^7\text{Li}$ value specified for the $\text{Li}_{0.04}\text{Na}_{0.96}\text{Cl}$
534 phase and a variation of the location of the input of the external groundwater Li source. An
535 overview of the simulated parameter combinations is given in Table 6.

536

537 **6.3. Model results and discussion**

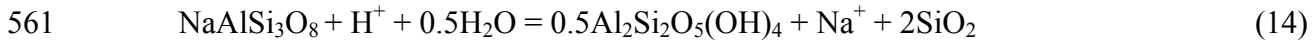
538

539 *6.3.1. General system behavior*

540 The general water-rock interaction progress along the 2000 m model domain is shown for a
541 general situation where the system is reactive enough to approach chemical equilibrium within
542 the model domain (Fig. 6). The profiles shown in Figure 6 are referred to such a general reaction
543 progress because it depends on the product of two unknown parameters such as reactive fracture
544 surface area (A_{rfrac}) and residence time (eq. (2)). If the system was more or less reactive, the
545 profiles except the temperature profile would be horizontally shifted towards lower or greater
546 distances, respectively, whereas the general profile shape would remain similar.

547 The relative change in mineral volume fraction demonstrates (Fig. 6c) that albite
548 dissolution and kaolinite precipitation are driving the general chemical system in addition to
549 quartz and calcite precipitation, as previously described for low-T crystalline groundwater
550 environments (Nordstrom et al., 1989; Grimaud et al., 1990; Trotignon et al., 1999; Gimeno et
551 al., 2014), and as reflected by the calculated mineral states (Table 4). In contrast, other primary
552 minerals (K-feldspar, chlorite, biotite, muscovite) show only minor volume changes whereas
553 goethite formation is restricted to the first grid block where pyrite is oxidized by oxygen
554 dissolved in the infiltrating meteoric water (Fig. 5). A prominent feature typical for the evolution
555 of crystalline groundwaters is the strong increase in pH from about 8.5 to 9.7, which at the
556 considered reaction progress occurs between 1000 to 1500 m along the model domain (Fig. 6a).
557 The increase in pH is correlated to the maximum albite dissolution and kaolinite formation (Fig.
558 6c). Across this interval, coupled albite dissolution and kaolinite precipitation is thus the main
559 reaction governing the pH increase:

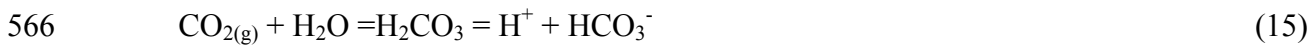
560



562

563 The actual driving force for reaction (14) is the supply of protons by the dissolution and
564 dissociation of atmospheric CO₂:

565



567

568 Prior to the strong pH increase, the system is controlled by calcite, i.e, by the initial
569 dissolution and subsequent precipitation caused by the calcite solubility decrease with increasing
570 temperature ($\text{Ca}^{2+}_{(\text{aq})} + \text{HCO}_3^{-}_{(\text{aq})} = \text{CaCO}_{3(\text{s})} + \text{H}^+$) (Fig. 6c). As the Ca^{2+} and HCO_3^{-}
571 concentrations decrease due to continuous calcite precipitation along the flow path, calcite
572 precipitation is diminished (Fig. 6b,c) and the pH is no longer controlled by calcite precipitation.
573 At this point, coupled albite dissolution and kaolinite precipitation is accelerated by the pH
574 dependence of the corresponding rates (*cf.* eq (3), Table 1) as well as by the linear temperature
575 increase along the flow path (Fig. 6a). As the system approaches equilibrium with respect to
576 albite (Fig. 6d), further albite dissolution and subsequent kaolinite precipitation are slowed down
577 and the pH becomes controlled by the speciation of dissolved Si ($\text{H}_4\text{SiO}_4 = \text{H}_3\text{SiO}_4^- + \text{H}^+$), which
578 becomes important above pH 9-9.5.

579 The maximum in coupled albite dissolution and kaolinite precipitation is reflected by the
580 Na concentration profile showing a maximum increase along the same interval as the strong pH
581 increase (Fig. 6b). In contrast, dissolved Si is controlled by the solubility of quartz, which
582 strongly increases above pH 9 when H_3SiO_4^- becomes the dominant Si species. Owing to the

583 linear temperature increase (Fig. 6a), Na^+ , Al^{3+} and Si concentrations are still increasing at the
584 downstream model boundary (Fig. 6b) because the solubility of albite and quartz are increasing
585 with temperature (Table 1). In turn, the pH slightly drops towards the model boundary because
586 of the temperature-dependence of the equilibrium pH of the simulated granitic system.

587

588 *Behavior of Li*

589 The modeled Li concentration of $\sim 0.6 \mu\text{g/L}$ inherited from biotite dissolution at the tunnel
590 level is very low (not shown) and demonstrates that only minor amounts of aqueous Li can be
591 derived from interaction between the infiltrating meteoric water and the BuMigIII rocks. Such a
592 minor Li contribution is consistent with a molar Mg/Li ratio in the BuMigIII water samples (<14 ,
593 Table 3) that is much lower than that in chloritized biotite forming the primary Li host of the
594 BuMigIII rock (ca. 65-85, Table 2). An additional Li input such as from the matrix porewater, an
595 external groundwater or an unknown mineral source is thus required to explain the observed Li
596 concentrations (Table 3).

597 For both Li influx scenarios modeled with the hypothetical $\text{Li}_{0.04}\text{Na}_{0.96}\text{Cl}$ phase (Fig. 5),
598 the model yields a strong $\delta^7\text{Li}$ increase between 1000-1500 m (Fig. 7a,b). At the considered
599 reaction progress, this interval corresponds to the maximum in kaolinite precipitation (Fig. 6c).
600 This suggests that Li isotope fractionation is coupled to kaolinite precipitation and that $\delta^7\text{Li}$
601 values are highly sensitive to the amount of kaolinite precipitation. Consequently, when kaolinite
602 precipitation slows down towards the downstream model boundary, the $\delta^7\text{Li}$ increase slows
603 down as well (Fig. 7b) or even starts to decrease (Fig. 7a) depending on the simulated scenario.

604 For the continuous Li influx scenario (Fig. 5a), the Li concentration increases over most
605 part of the domain because the Li influx outpaces the Li uptake by secondary kaolinite

606 precipitation, except for a short interval where kaolinite precipitation is maximal (Fig. 7a).
607 Consequently, for this scenario, $\delta^7\text{Li}$ is positively correlated to the Li concentration with the
608 exception of the downstream model boundary where $\delta^7\text{Li}$ is decreasing (Fig. 7a,c) because the Li
609 load in the fracture fluid becomes dominated by the ongoing Li influx with a $\delta^7\text{Li}$ of 8.7‰. For
610 the mixing scenario (Fig. 5b), the Li concentration decreases after the single point Li input
611 yielding throughout a negative correlation with $\delta^7\text{Li}$ (Fig. 7b,c).

612

613 *6.3.2. Application to BuMigIII groundwater*

614 The observation that only the mixing scenario yields a negative correlation between $\delta^7\text{Li}$
615 and the Li concentration, as observed in BuMigIII groundwater (Fig. 2), suggests that Li is
616 inherited from a discrete rather than from a continuous Li influx. Whereas mixing with an
617 external groundwater is a likely candidate for single point Li influx, it is also possible that it
618 occurred from a not yet identified rock type enriched in Li-bearing mineral(s), with a
619 composition that is significantly different from that of the BuMigIII rock exposed at the tunnel
620 level.

621 To further apply the mixing scenario (Fig. 5b) to the BuMigIII system, the model was run
622 for a variable reaction progress along the 2000 m long flow path by varying the flow velocity
623 while keeping the reactive fracture surface area constant. Consequently, steady state major
624 species concentrations computed for the tunnel level ($z = -2000$ m) are plotted against the pH to
625 illustrate their dependence on the overall reaction progress and to compare them with measured
626 BuMigIII groundwater data (Fig. 8). Although the fits are not perfect, the fact that the order of
627 magnitude is reproducible suggests that the model captures the governing mineral reactions.

628 Differences between modeled and observed concentrations are likely inherited from the
629 assumptions of constant flow velocity and homogeneous mineralogy along the flow path.

630

631 *Li system*

632 The sensitivity of our model parameters on the Li system was tested by comparing
633 measured $\delta^7\text{Li}$ and Li concentrations with computed steady state values obtained at the tunnel
634 level for a variable reaction progress along the flow path and for 7 combinations of Li isotope
635 enrichment factors, maximum Li concentrations in kaolinite, and kaolinite precipitation rate
636 constants. Figure 9 illustrates that all varied parameters have an effect on the Li concentration
637 and/or on $\delta^7\text{Li}$. Higher amounts of Li incorporation into kaolinite as well as higher amounts of
638 kaolinite precipitation increase the $\delta^7\text{Li}$ value and decrease the Li concentration for a given
639 reaction progress (i.e., pH) because both parameters increase the ratio between the Li uptake by
640 kaolinite and the external Li input. Increasing the Li isotope enrichment factor also yields an
641 increase in the $\delta^7\text{Li}$ value for a given reaction progress (i.e., pH), but does obviously not change
642 the Li concentration. The sensitivity analyses carried out for the location of the single point Li
643 influx yielded only minor dependence as long as it occurred before the system evolved to the
644 maximum kaolinite formation rate (not shown).

645 In general, simulations performed for the mixing scenario approximate the observed pH
646 dependence of measured $\delta^7\text{Li}$ values (Fig. 9), although in a non-linear manner, and the observed
647 Li concentrations can be reproduced. The best match between modeled and measured data is
648 obtained for a Li isotope enrichment factor of -50‰, a maximum Li concentration in kaolinite of
649 75 $\mu\text{g/g}$ and a slightly reduced kaolinite precipitation rate constant (i.e., simulation M7; Fig. 9).
650 A similar fit, however, is obtained when setting the $\delta^7\text{Li}$ value of the single point Li source to 1.7

651 ‰ while limiting the amount of Li in kaolinite to 50 µg/g (Fig. 10). The observation that
652 different parameter combinations result in similar good fits demonstrates that the system is
653 under-determined and that not all parameters affecting the Li system can be calibrated in a
654 quantitative way. The observed negative correlation between $\delta^7\text{Li}$ and Li concentration,
655 however, can only be approximated if the Li isotope enrichment factor is as high as -50‰ (Fig.
656 9). An enrichment factor of -50‰ also corresponds to that obtained from the Rayleigh-type
657 model (Fig. 2d). This is an interesting observation because $\epsilon=-50\text{‰}$ is clearly outside the range
658 of Li isotope enrichment factor reported or inferred for secondary mineral precipitation (≈ -10 to
659 -30‰) (Zhang et al., 1998; Huh et al., 2001; Pistiner and Henderson, 2003; Kisakürek et al.,
660 2005; Pogge von Strandmann et al., 2006; Vigier et al., 2008; Pogge von Strandmann et al.,
661 2010), although vigorous determination of the temperature-dependence of Li isotope
662 fractionation involving mineral precipitation have so far only been reported for Li incorporation
663 during smectite precipitation (Vigier et al., 2008). Since a contribution from diffusive Li isotope
664 fractionation would yield an even higher intrinsic enrichment factor and an anthropogenic Li
665 contamination is unlikely, the reason for the high apparent Li isotope enrichment factor is
666 unclear and further research is required to unravel whether this is related to the slow flow rates
667 and/or alkaline conditions of our system.

668 Overall, our model results reveal that the large $\delta^7\text{Li}$ variation observed in BuMigIII
669 groundwater samples (10-41‰) are related to their pH range of 9.3 to 9.8. Over this pH window,
670 the amount of coupled albite dissolution and kaolinite precipitation is at its maximum (Fig. 6).
671 Consequently, a variation in reaction progress along the infiltration path (e.g., variable residence
672 time) strongly affects the amount of Li-bearing kaolinite precipitation and thus the $\delta^7\text{Li}$ value.
673 Simulation results also reveal that the observed Li isotope fractionation is independent of the

674 origin of Li (ad-mixing of external groundwater, in-diffusion from porewater, dissolution of
675 unidentified minerals) as long as this addition occurred before the infiltrating meteoric water
676 evolved to its maximum kaolinite formation. This latter point further argues against a continuous
677 addition of Li by diffusion from the porewater as there is no reason why such addition should
678 stop at a certain point along the flowpath in the same rock unit.

679

680 *6.3.3. Application to Bristner Granite groundwater*

681 Based on the finding that the mixing scenario (Fig. 5b) can explain the $\delta^7\text{Li}$ variation
682 observed in BuMigIII samples (Table 3), the same modeling approach was used to explore the
683 sensitivity of $\delta^7\text{Li}$ on the Li concentration and to particularly test whether the absence of $\delta^7\text{Li}$
684 variation in Bristner Granite groundwater is simply caused by its high Li concentration (Table 3).
685 To do so, the mixing scenario (Fig. 5b) was run by setting the Li concentration of the simulated
686 groundwater mixture to 0.017, 0.08, 0.17, and 1.7 mg/L, whereas the other parameters were kept
687 constant at the values used in simulation M7 (Table 6). As can be seen from Figure 11, the
688 simulated $\delta^7\text{Li}$ values strongly depend on the Li concentration in the groundwater. At a Li
689 concentration representing the range of Bristner Granite groundwater (1.7 mg/L), the predicted
690 $\delta^7\text{Li}$ value does not differ from the value specified for the single point Li influx ($\delta^7\text{Li}=8.7\text{‰}$). A
691 change in the $\delta^7\text{Li}$ values is only obtained if the Li concentration in the groundwater is lowered
692 by a factor of 10 or more. The reason for these effects lies in the amount of Li that was allowed
693 to be incorporated into precipitating kaolinite (75 $\mu\text{g/g}$). Accordingly, the ratio between Li that is
694 incorporated into kaolinite and Li obtained from the single point influx decreases with increasing
695 Li concentration in such influx. Because this ratio is also reflected in the $\delta^7\text{Li}$ value, the
696 computed $\delta^7\text{Li}$ values become lower as the concentration of Li from the influx increases. The

697 ability of the model to predict the absence of $\delta^7\text{Li}$ at high Li concentration supports the existence
698 of a maximum amount of Li that can be structurally incorporated into precipitating kaolinite,
699 which is in agreement with mineralogical and experimental findings (Tardy et al., 1972;
700 Decarreau et al., 2012; Vigier and Godd ris, 2015). Such limitation further constitutes the likely
701 reason for the low $\delta^7\text{Li}$ values and absence of $\delta^7\text{Li}$ variation observed for the Bristner Granite
702 groundwater where the Li concentration is up to 500 times higher than in BuMigIII groundwater
703 (Table 3).

704

705 **7. IMPLICATIONS FOR USING $\delta^7\text{Li}$ AS A WATER-ROCK INTERACTION PROXY**

706 The comparison between analytical and simulation results confirms that for a relatively
707 simple hydrological system, aqueous $\delta^7\text{Li}$ is controlled by the cumulative amount of Li-bearing
708 secondary mineral formation in relation to the Li release from primary mineral or other Li
709 sources (Wanner et al., 2014; Pogge von Strandmann et al., 2016). Because secondary mineral
710 formation is coupled to the dissolution of primary minerals, $\delta^7\text{Li}$ may be used in conjunction
711 with major species concentrations to estimate mineral reaction rates using modeling approaches
712 such as the one presented here. However, even for mono-lithological systems, an accurate
713 quantification of these rates based on $\delta^7\text{Li}$ remains challenging. The first issue is that $\delta^7\text{Li}$ values
714 are strongly affected by the reactivity of system (Fig. 9), which is controlled by the flow velocity
715 (or the residence time, respectively), and the reactive surface areas. Secondly, dissolution and
716 precipitation rates of silicate minerals are highly pH and temperature dependent (Fig. 6),
717 demonstrating that the spatial temperature and pH distribution must be known to constrain
718 reaction rates for a given flow system. Finally, our sensitivity analyses suggest that aqueous $\delta^7\text{Li}$
719 values are controlled by the amount of Li that can be taken up by secondary minerals, as well as

720 the corresponding fractionation factor (Fig. 9). None of these parameters are fully characterized
721 for the entire suite of Li bearing secondary minerals. For well-constrained hydrogeological
722 systems, however, the listed challenges are likely resolved in the future once more experimental
723 data will become available. Our model results based on actual data from a crystalline
724 groundwater environment at elevated temperatures and including kaolinite precipitation indicate
725 that $\delta^7\text{Li}$ values might be especially useful to better constrain the formation rate of secondary
726 minerals for which kinetic data are still scarce (Yang and Steefel, 2008 and references therein).
727 Moreover, the strong $\delta^7\text{Li}$ variation observed at temperatures above those at the Earth's surface
728 (Table 3) demonstrates the potential for using $\delta^7\text{Li}$ as water-rock interaction proxy at elevated
729 temperatures. If the sensitivity of $\delta^7\text{Li}$ on the Li concentration, however, is as high as inferred
730 from Figure 11, the use of $\delta^7\text{Li}$ to constrain mineral reaction rates is restricted to systems with
731 low Li concentrations, which does usually not apply for hydro-geothermal systems (Chan et al.,
732 1994; Millot and Négrel, 2007; Millot et al., 2010a; Sanjuan et al., 2014; Sanjuan et al., 2016).

733 In contrast to well-defined systems, we suspect that quantifying continental silicate
734 weathering rates through time based on the Cenozoic seawater $\delta^7\text{Li}$ record and the reconstructed
735 riverine $\delta^7\text{Li}$ evolution (Misra and Froelich, 2012; Li and West, 2014; Vigier and Godd ris,
736 2015) will remain challenging. Because rivers are characterized by specific subsurface residence
737 time distributions, the identified sensitivity of $\delta^7\text{Li}$ on the subsurface residence time implies that
738 an accurate estimation requires capturing of subsurface residence time variations through time
739 (e.g., discharge variations) under a changing climate and at an increasing tectonic activity (Misra
740 and Froelich, 2012; Vigier and Godd ris, 2015). Another major challenge is that $\delta^7\text{Li}$ variations
741 are likely controlled by the corresponding Li concentration such as inferred by our simulation
742 results (Figs. 11) and likely manifested by the absence of $\delta^7\text{Li}$ variation in the Bristner Granite

743 groundwater. This apparent sensitivity of $\delta^7\text{Li}$ on the Li concentration implies reconstructing the
744 evolution of the continental Li flux distribution through time in addition to subsurface residence
745 variations. In this context, first Cenozoic continental Li flux reconstructions have been presented
746 recently (Li and West, 2014; Vigier and Godd ris, 2015).

747

748 **8. SUMMARY AND CONCLUSIONS**

749 The use of Li isotope measurements for tracking water-rock interaction in fractured
750 crystalline aquifers at temperatures of up to 43 C was assessed by performing Li isotope
751 measurements on 17 groundwater samples collected during drilling of the new Gotthard rail base
752 tunnel in Switzerland. A particular effort was made to match $\delta^7\text{Li}$ values as well as major species
753 concentrations by reactive transport model simulations using the code TOUGHREACT V3. In
754 doing so, the possibility of defining a maximum amount of a trace element that is incorporated
755 into the structure of a precipitating mineral was added as a new capability to TOUGHREACT
756 V3. The main conclusions from this study are:

- 757 1. The alteration of fracture surfaces by a circulating fluid may lead to a strong variation of
758 $\delta^7\text{Li}$ values at temperatures of up to 43 C. A strong $\delta^7\text{Li}$ variation, however, was only
759 observed if the Li concentration was low (0.01-0.02 mg/L). For high Li concentrations on
760 the order of 1-4 mg/L, no variation was observed suggesting that the amount of Li that
761 can be incorporated into secondary minerals is limited and that the use of $\delta^7\text{Li}$ values as a
762 proxy for water-rock interaction is restricted to low Li concentrations.
- 763 2. Li uptake by kaolinite precipitation or by the precipitation of other Al-bearing phases
764 forms the key process to cause Li isotope fractionation in fractured crystalline aquifers
765 characterized by a granitic mineralogical composition. Our data suggests that under slow

766 flow conditions (<10 m/year), at temperatures <50 °C, and alkaline conditions (pH>9),
767 this Li uptake is associated with a very large Li isotope fractionation factor ($\epsilon \approx -50 \text{ ‰}$).

768 3. For the samples with low Li concentrations, $\delta^7\text{Li}$ values are mainly controlled by the
769 cumulative amount of kaolinite precipitation occurring along the flow path.
770 Consequently, aqueous $\delta^7\text{Li}$ values are sensitive to fluid residence times, reactive fracture
771 surface areas, and pH values, all controlling overall silicate mineral reaction rates.

772 4. Incorporating the fate of Li isotopes into fully coupled reactive transport model
773 simulations allows a predictive understanding of measured Li isotope ratios. For simple
774 and well-defined systems with known residence times and low Li concentrations, $\delta^7\text{Li}$
775 values may help to quantify mineral reaction rates and associated parameters (e.g.,
776 reactive surface area). An accurate quantification, however, currently suffers from the
777 lack of thermodynamic data such as the temperature dependent amount of Li that can be
778 incorporated into secondary minerals as well as corresponding fractionation factors.

779 5. In crystalline aquifers with high Li concentrations such as in the Bristner Granite,
780 groundwater Li is likely inherited from an ancient hydrothermal fluid still residing in the
781 pore space of the intact rock matrix.

782

783 **ACKNOWLEDGMENTS**

784 This work is dedicated to H.-J. (Jöggu) Ziegler, head geologist of the Gotthard rail base tunnel
785 who brought CW first into contact with the intriguing water samples from the Gotthard rail base
786 tunnel and who passed away on the same day CW started to look for available samples. CW was
787 supported by the Swiss Competence Center for Energy Research-Supply of Electricity (SCCER-
788 SOE). PPvS and Li isotope analyses were funded by NERC Advanced Research Fellowship

789 NE/I020571/2. Finally, we thank the associated editor, Horst Marschall, and 4 anonymous
790 reviewers for their constructive comments that greatly improved the manuscript.

791

792

793 **FIGURE CAPTIONS**

794 Figure 1: Geological cross section through the Amsteg section of the Gotthard rail base tunnel
795 (modified from Bucher et al., 2012). The two sections from which water and rock samples were
796 taken for Li concentration and Li isotope measurements are highlighted.

797

798 Figure 2: $\delta^7\text{Li}$ values of BuMigIII water samples plotted against the pH (**a**), the [Li] (**b**), and the
799 molar Li/Na ratio (**c**). The shown correlations were obtained by not considering the two samples
800 with special features (e.g., anhydrite dissolution and low temperature). (**d**) Rayleigh model
801 ($\delta^7\text{Li} = \delta^7\text{Li}_{\text{ini}} + 1000(f^{\alpha-1}) - 1000$) using an enrichment factor ϵ of -50‰ ($\epsilon = (\alpha - 1) * 1000$), an initial
802 $\delta^7\text{Li}$ of 7‰ and a [Li] of 17 $\mu\text{g/L}$ at $f=1$.

803

804 Figure 3: Excellent linear correlation between Li^+ and Cl^- observed for groundwater samples
805 collected from the Bristner Granite.

806

807 Figure 4: Comparison between experimentally determined and tabulated $\log(K)$ values for the
808 following kaolinite hydrolysis reaction: $\text{Al}_2\text{Si}_2\text{O}_5(\text{OH})_4 + 3\text{H}_2\text{O} = 2\text{Al}(\text{OH})_4^- + 2\text{SiO}_2 + 2\text{H}^+$.

809

810 Figure 5: Li influx scenarios and corresponding model setups for simulating the infiltration of
811 meteoric water into the BuMigIII rock column above the tunnel.

812

813 Figure 6: General behaviour of the simulated interaction between infiltrating meteoric water and
814 the granitic BuMigIII. Steady state profiles along the model are shown for temperature and pH
815 **(a)**, total major species concentrations **(b)**, changes in mineral volume fractions relative to t=0
816 after a simulated time of 10'000 years **(c)**, and saturation indices of selected mineral phases **(d)**.
817 All profiles refer to a general situation where chemical equilibrium is approached along the flow
818 path (e.g., $v=1$ m/year and $A_{frac}=0.01$ m²/m³_{fractured_medium}).

819

820 Figure 7: General behavior of Li in the two Li influx scenarios (Fig. 5) at the same reaction
821 progress as shown in Fig. 6. **(a)** continuous Li influx scenario. **(b)** mixing scenario. **(c)**
822 correlation between $\delta^7\text{Li}$ and Li. Results correspond to an Li isotope enrichment and maximum
823 amount of Li in kaolinite of -50‰ and 75 $\mu\text{g/g}$, respectively (simulations C1 and M3, Table 6).

824

825 Figure 8: Major species concentrations computed for the tunnel level and plotted against the pH
826 to illustrate their behavior with respect to a variable reaction progress along the model domain
827 (e.g., variable residence time). Also shown are corresponding measurements of BuMigIII
828 groundwater samples.

829

830 Figure 9: Sensitivity analyses performed for the mixing scenario (Fig. 5b). **(a)** compares
831 measured $\delta^7\text{Li}$ and [Li] with values computed as a function of the reaction progress along the
832 model domain (i.e., as a function of pH/residence time) and for a variable maximum Li
833 concentration in kaolinite. **(b)** shows the same parameters as in **(a)**, but for a varying Li isotope

834 enrichment factor. In (c) the comparison between model and observations is shown for a varying
835 kaolinite precipitation rate.

836

837 Figure 10. Two parameter combinations that can well approximate the correlations between $\delta^7\text{Li}$,
838 Li and pH observed in the BuMigIII groundwater when running the model for a variable reaction
839 progress (e.g., by varying the residence time).

840

841 Figure 11: Sensitivity of $\delta^7\text{Li}$ values on the aqueous Li concentration. Computed Li
842 concentration (a) and $\delta^7\text{Li}$ (b) at the tunnel level are shown for a varying Li concentration of the
843 simulated groundwater mixture (Fig. 5b) as a function of the reaction progress (i.e., pH).

844

845 REFERENCES

- 846 Abrecht J. (1994) Geologic units of the Aarmassif and their pre-Alpine rock associations: a
847 critical review. *Schweizerische Mineralogische und Petrographische Mitteilungen* **74**, 5-
848 27.
- 849 Alt-Epping P., Diamond L. W., Häring M. O., Ladner F. and Meier D. B. (2013) Prediction of
850 water-rock interaction and porosity evolution in a granitoid-hosted enhanced geothermal
851 system, using constraints from the 5 km Basel-1 well. *Appl. Geochem.* **38**, 121-133.
- 852 Berner R. A., Lasaga A. C. and Garrels R. M. (1983) The carbonate-silicate geochemical cycle
853 and its effect on atmospheric carbon-dioxide over the past 100 million years. *Am. J. Sci.*
854 **283**, 641-683.
- 855 Bouchez J., Von Blanckenburg F. and Schuessler J. A. (2013) Modeling novel stable isotope
856 ratios in the weathering zone. *Am. J. Sci.* **313**, 267-308.
- 857 Bourg I. C. and Sposito G. (2007) Molecular dynamics simulations of kinetic isotope
858 fractionation during the diffusion of ionic species in liquid water. *Geochim. Cosmochim.*
859 *Acta* **71**, 5583-5589.
- 860 Brown S. T., Kennedy B. M., DePaolo D. J., Hurwitz S. and Evans W. C. (2013) Ca, Sr, O and D
861 isotope approach to defining the chemical evolution of hydrothermal fluids: Example from
862 Long Valley, CA, USA. *Geochim. Cosmochim. Acta* **122**, 209-225.
- 863 Bucher K., Stober I. and Seelig U. (2012) Water deep inside the mountains: Unique water
864 samples from the Gotthard rail base tunnel, Switzerland. *Chem. Geol.* **334**, 240-253.
- 865 Caine J. S. and Tomusiak S. R. A. (2003) Brittle structures and their role in controlling porosity
866 and permeability in a complex Precambrian crystalline-rock aquifer system in the Colorado
867 Rocky Mountain front range. *Geological Society of America Bulletin* **115**, 1410-1424.

- 868 Chan L.-H., Edmond J. M. and Thompson G. (1993) A lithium isotope study of hot springs and
869 metabasalts from Mid-Ocean Ridge Hydrothermal Systems. *Journal of Geophysical*
870 *Research: Solid Earth* **98**, 9653-9659.
- 871 Chan L.-H., Gieskes J. M., Chen-Feng Y. and Edmond J. M. (1994) Lithium isotope
872 geochemistry of sediments and hydrothermal fluids of the Guaymas Basin, Gulf of
873 California. *Geochim. Cosmochim. Acta* **58**, 4443-4454.
- 874 Decarreau A., Vigier N., Pálková H., Petit S., Vieillard P. and Fontaine C. (2012) Partitioning of
875 lithium between smectite and solution: An experimental approach. *Geochim. Cosmochim.*
876 *Acta* **85**, 314-325.
- 877 Dellinger M., Gaillardet J., Bouchez J., Calmels D., Louvat P., Dosseto A., Gorge C., Alanoca L.
878 and Maurice L. (2015) Riverine Li isotope fractionation in the Amazon River basin
879 controlled by the weathering regimes. *Geochim. Cosmochim. Acta* **164**, 71-93.
- 880 DePaolo D. J. (2006) Isotopic effects in fracture-dominated reactive fluid–rock systems.
881 *Geochim. Cosmochim. Acta* **70**, 1077-1096.
- 882 Devidal J.-L., Dandurand J.-L. and Gout R. (1996) Gibbs free energy of formation of kaolinite
883 from solubility measurement in basic solution between 60 and 170 °C. *Geochim.*
884 *Cosmochim. Acta* **60**, 553-564.
- 885 Francois L. M. and Godderis Y. (1998) Isotopic constraints on the Cenozoic evolution of the
886 carbon cycle. *Chem. Geol.* **145**, 177-212.
- 887 Gimeno M. J., Auqué L. F., Acero P. and Gómez J. B. (2014) Hydrogeochemical
888 characterisation and modelling of groundwaters in a potential geological repository for
889 spent nuclear fuel in crystalline rocks (Laxemar, Sweden). *Appl. Geochem.* **45**, 50-71.
- 890 Gislason S. R., Arnorsson S. and Armannsson H. (1996) Chemical weathering of basalt in
891 Southwest Iceland; effects of runoff, age of rocks and vegetative/glacial cover. *Am. J. Sci.*
892 **296**, 837-907.
- 893 Grimaud D., Beaucaire C. and Michard G. (1990) Modelling of the evolution of ground waters in
894 a granite system at low temperature: the Stripa ground waters, Sweden. *Appl. Geochem.* **5**,
895 515-525.
- 896 Guillong M., Meier D. L., Allan M. M., Heinrich C. A. and Yardley B. W. D. (2008) SILLS: A
897 MATLAB-based program for the reduction of laser ablation ICP-MS data of homogeneous
898 materials and inclusions, in: Sylvester, P. (Ed.), *Laser ablation ICP-MS in the Earth*
899 *Sciences: current practices and outstanding issues*, pp. 328-333.
- 900 Henchiri S., Clergue C., Dellinger M., Gaillardet J., Louvat P. and Bouchez J. (2014) The
901 Influence of Hydrothermal Activity on the Li Isotopic Signature of Rivers Draining
902 Volcanic Areas. *Proc. Earth Planet. Sci.* **10**, 223-230.
- 903 Huh Y., Chan L. H., Zhang L. and Edmond J. M. (1998) Lithium and its isotopes in major world
904 rivers: Implications for weathering and the oceanic budget. *Geochim. Cosmochim. Acta* **62**,
905 2039-2051.
- 906 Huh Y., Chan L. H. and Edmond J. M. (2001) Lithium isotopes as a probe of weathering
907 processes: Orinoco River. *Earth Planet. Sci. Lett.* **194**, 189-199.
- 908 Huh Y., Chan L. H. and Chadwick O. A. (2004) Behavior of lithium and its isotopes during
909 weathering of Hawaiian basalt. *Geochem. Geophys. Geosy.* **5**.
- 910 Kisakürek B., James R. H. and Harris N. B. W. (2005) Li and $\delta^7\text{Li}$ in Himalayan rivers: Proxies
911 for silicate weathering? *Earth Planet. Sci. Lett.* **237**, 387-401.
- 912 Kittrick J. A. (1966) Free energy of formation of kaolinite from solubility measurements.
913 *American Mineralogist* **51**, 1457-&.

- 914 Labhart T. P. (1999) Aarmassiv, Gotthardmassiv und Tavetscher Zwischenmassiv: Aufbau und
915 Entstehungsgeschichte, in: Loew, S., Wyss, R. (Eds.), Symposium Geologie Alptransit,
916 Zürich. Balkema, Rotterdam, pp. 31-43.
- 917 Lasaga A. C. (1984) Chemical kinetics of water-rock interactions. *J. Geoph. Res.* **89**, 4009-4025.
- 918 Lemarchand E., Chabaux F., Vigier N., Millot R. and Pierret M.-C. (2010) Lithium isotope
919 systematics in a forested granitic catchment (Strengbach, Vosges Mountains, France).
920 *Geochim. Cosmochim. Acta* **74**, 4612-4628.
- 921 Li G. and West A. J. (2014) Evolution of Cenozoic seawater lithium isotopes: Coupling of global
922 denudation regime and shifting seawater sinks. *Earth Planet. Sci. Lett.* **401**, 284-293.
- 923 Liu X.-M., Wanner C., Rudnick R. L. and McDonough W. F. (2015) Processes controlling $\delta^7\text{Li}$
924 in rivers illuminated by study of streams and groundwaters draining basalts. *Earth Planet.*
925 *Sci. Lett.* **409**, 212-224.
- 926 MacQuarrie K. T. B. and Mayer K. U. (2005) Reactive transport modeling in fractured rock: A
927 state-of-the-science review. *Earth-Sci. Rev.* **72**, 189-227.
- 928 Marschall H. R., Pogge von Strandmann P. A. E., Seitz H.-M., Elliott T. and Niu Y. (2007) The
929 lithium isotopic composition of orogenic eclogites and deep subducted slabs. *Earth Planet.*
930 *Sci. Lett.* **262**, 563-580.
- 931 Masset O. and Loew S. (2013) Quantitative hydraulic analysis of pre-drillings and inflows to the
932 Gotthard Base Tunnel (Sedrun Lot, Switzerland). *Eng. Geol.* **164**, 50-66.
- 933 May H. M., Klennburgh D. G., Helmke P. A. and Jackson M. L. (1986) Aqueous dissolution,
934 solubilities and thermodynamic stabilities of common aluminosilicate clay minerals:
935 Kaolinite and smectites. *Geochim. Cosmochim. Acta* **50**, 1667-1677.
- 936 Mazurek M., Jakob A. and Bossart P. (2003) Solute transport in crystalline rocks at Äspö — I:
937 Geological basis and model calibration. *J. Contam. Hydrol.* **61**, 157-174.
- 938 Michard G., Pearson Jr F. J. and Gautschi A. (1996) Chemical evolution of waters during long
939 term interaction with granitic rocks in northern Switzerland. *Appl. Geochem.* **11**, 757-774.
- 940 Millot R. and Négrel P. (2007) Multi-isotopic tracing ($\delta^7\text{Li}$, $\delta^{11}\text{B}$, $^{87}\text{Sr}/^{86}\text{Sr}$) and chemical
941 geothermometry: evidence from hydro-geothermal systems in France. *Chem. Geol.* **244**,
942 664-678.
- 943 Millot R., Scaillet B. and Sanjuan B. (2010a) Lithium isotopes in island arc geothermal systems:
944 Guadeloupe, Martinique (French West Indies) and experimental approach. *Geochim.*
945 *Cosmochim. Acta* **74**, 1852-1871.
- 946 Millot R., Vigier N. and Gaillardet J. (2010b) Behaviour of lithium and its isotopes during
947 weathering in the Mackenzie Basin, Canada. *Geochim. Cosmochim. Acta* **74**, 3897-3912.
- 948 Misra S. and Froelich P. N. (2012) Lithium isotope history of Cenozoic seawater: changes in
949 silicate weathering and reverse weathering. *Science* **335**, 818-823.
- 950 Molinero J., Raposo J. R., Galíndez J. M., Arcos D. and Guimerá J. (2008) Coupled
951 hydrogeological and reactive transport modelling of the Simpevarp area (Sweden). *Appl.*
952 *Geochem.* **23**, 1957-1981.
- 953 Nagy K. L., Blum A. E. and Lasaga A. C. (1991) Dissolution and precipitation kinetics of
954 kaolinite at 80 degrees C and pH 3; the dependence on solution saturation state. *Am. J. Sci.*
955 **291**, 649-686.
- 956 Nordstrom D. K., Ball J. W., Donahoe R. J. and Whittmore D. (1989) Groundwater chemistry
957 and water-rock interactions at Stripa. *Geochim. Cosmochim. Acta* **53**, 1727-1740.
- 958 Palandri J. L. and Kharaka Y. K. (2004) A compilation of rate parameters of water-mineral
959 interaction kinetics for application to geochemical modeling. US Geological Survey.

- 960 Pettke T., Oberli F., Audétat A., Guillong M., Simon A. C., Hanley J. J. and Klemm L. M.
 961 (2012) Recent developments in element concentration and isotope ratio analysis of
 962 individual fluid inclusions by laser ablation single and multiple collector ICP-MS. *Ore*
 963 *Geology Reviews* **44**, 10-38.
- 964 Pistiner J. S. and Henderson G. M. (2003) Lithium-isotope fractionation during continental
 965 weathering processes. *Earth Planet. Sci. Lett.* **214**, 327-339.
- 966 Pogge von Strandmann P. A. E., Burton K. W., James R. H., van Calsteren P., Gíslason S. R. and
 967 Mokadem F. (2006) Riverine behaviour of uranium and lithium isotopes in an actively
 968 glaciated basaltic terrain. *Earth Planet. Sci. Lett.* **251**, 134-147.
- 969 Pogge von Strandmann P. A. E., Burton K. W., James R. H., van Calsteren P. and Gíslason S. R.
 970 (2010) Assessing the role of climate on uranium and lithium isotope behaviour in rivers
 971 draining a basaltic terrain. *Chem. Geol.* **270**, 227-239.
- 972 Pogge von Strandmann P. A. E., Elliott T., Marschall H. R., Coath C., Lai Y.-J., Jeffcoate A. B.
 973 and Ionov D. A. (2011) Variations of Li and Mg isotope ratios in bulk chondrites and
 974 mantle xenoliths. *Geochim. Cosmochim. Acta* **75**, 5247-5268.
- 975 Pogge von Strandmann P. A. E., Porcelli D., James R. H., van Calsteren P., Schaefer B.,
 976 Cartwright I., Reynolds B. C. and Burton K. W. (2014) Chemical weathering processes in
 977 the Great Artesian Basin: Evidence from lithium and silicon isotopes. *Earth Planet. Sci.*
 978 *Lett.* **406**, 24-36.
- 979 Pogge von Strandmann P. A. E. and Henderson G. M. (2015) The Li isotope response to
 980 mountain uplift. *Geology* **43**, 67-70.
- 981 Pogge von Strandmann P. A. E., Burton K. W., Opfergelt S., Eiríksdóttir E. S., Murphy M. J.,
 982 Einarsson A. and Gíslason S. R. (2016) The effect of hydrothermal spring weathering
 983 processes and primary productivity on lithium isotopes: Lake Myvatn, Iceland. *Chem.*
 984 *Geol.* **in press**, DOI: <http://dx.doi.org/10.1016/j.chemgeo.2016.02.026>.
- 985 Polzer W. L. and Hem J. D. (1965) The dissolution of kaolinite. *J. Geoph. Res.* **70**, 6233-6240.
- 986 Reed M. and Palandri J. L. (2006) SOLTHERM.H06, a database of equilibrium constants for
 987 minerals and aqueous species. Available from the authors, University of Oregon, Eugene,
 988 USA.
- 989 Reesman A. L. and Keller W. D. (1968) Aqueous solubility studies of high-alumina and clay
 990 minerals. *American Mineralogist* **53**, 929-&.
- 991 Richter F. M., Mendybaev R. A., Christensen J. N., Hutcheon I. D., Williams R. W., Sturchio N.
 992 C. and Beloso Jr A. D. (2006) Kinetic isotopic fractionation during diffusion of ionic
 993 species in water. *Geochim. Cosmochim. Acta* **70**, 277-289.
- 994 Sanjuan B., Millot R., Ásmundsson R., Brach M. and Giroud N. (2014) Use of two new Na/Li
 995 geothermometric relationships for geothermal fluids in volcanic environments. *Chem.*
 996 *Geol.* **389**, 60-81.
- 997 Sanjuan B., Millot R., Innocent C., Dezayes C., Scheiber J. and Brach M. (2016) Major
 998 geochemical characteristics of geothermal brines from the Upper Rhine Graben granitic
 999 basement with constraints on temperature and circulation. *Chem. Geol.* **428**, 27-47.
- 1000 Schaltegger U. (1994) Unravelling the pre-Mesozoic history of the Aar and Gotthard massifs
 1001 (Central Alps) by isotopic dating — a review. *Schweizerische Mineralogische und*
 1002 *Petrographische Mitteilungen* **74**, 41-51.
- 1003 Schwertmann U. (1988) Occurrence and Formation of Iron Oxides in Various
 1004 Pedoenvironments, in: Stucki, J.W., Goodman, B.A., Schwertmann, U. (Eds.), *Iron in Soils*
 1005 *and Clay Minerals*. Springer Netherlands, Dordrecht, pp. 267-308.

- 1006 Seelig U. and Bucher K. (2010) Halogens in water from the crystalline basement of the Gotthard
1007 rail base tunnel (central Alps). *Geochim. Cosmochim. Acta* **74**, 2581-2595.
- 1008 Singleton M. J., Sonnenthal E. L., Conrad M. E., DePaolo D. J. and Gee G. W. (2005)
1009 Multiphase reactive transport modeling of seasonal infiltration events and stable isotope
1010 fractionation in unsaturated zone pore water and vapor at the Hanford site. *Vadose Zone J.*
1011 **3**, 775-785.
- 1012 Sonnenthal E. L., Spycher N., Apps J. A. and Simmons A. (1998) Thermo-hydro-chemical
1013 predictive analysis for the drift-scale heater test. Lawrence Berkeley National Laboratory
1014 report **SPY289M4**.
- 1015 Sonnenthal E. L., Ito A., Spycher N., Yui M., Apps J. A., Sugita Y., Conrad M. E. and
1016 Kawakami S. (2005) Approaches to modeling coupled thermal, hydrological and chemical
1017 processes in the Drift Scale Heater Test at Yucca Mountain. *Int. J. Rock Mech. Min. Sci.*
1018 **42**, 698-719.
- 1019 Spandler C., Pettke T. and Rubatto D. (2011) Internal and External Fluid Sources for Eclogite-
1020 facies Veins in the Monviso Meta-ophiolite, Western Alps: Implications for Fluid Flow in
1021 Subduction Zones. *J. Petrol.* **52**, 1207-1236
- 1022 Steefel C. I., Appelo C. A. J., Arora B., Jacques D., Kalbacher T., Kolditz O., Lagneau V.,
1023 Lichtner P. C., Mayer K. U., Meussen H., Molins S., Moulton D., Parkhurst D. L., Shao H.,
1024 Simunek J., Spycher N., Yabusaki S. and Yeh G. T. (2015) Reactive transport codes for
1025 subsurface environmental simulation. *Comput. Geosci.* **19**, 445-478.
- 1026 Stober I. and Bucher K. (2015) Hydraulic conductivity of fractured upper crust: insights from
1027 hydraulic tests in boreholes and fluid-rock interaction in crystalline basement rocks.
1028 *Geofluids* **15**, 161-178.
- 1029 Tardy Y., Trauth N. and Kremp G. (1972) Lithium in clay-minerals of sediments and soils.
1030 *Geochim. Cosmochim. Acta* **36**, 397-&.
- 1031 Teng F.-Z., Rudnick R. L., McDonough W. F. and Wu F.-Y. (2009) Lithium isotopic systematics
1032 of A-type granites and their mafic enclaves: Further constraints on the Li isotopic
1033 composition of the continental crust. *Chem. Geol.* **262**, 370-379.
- 1034 Trotignon L., Beaucaire C., Louvat D. and Jean-François A. (1999) Equilibrium geochemical
1035 modelling of Äspö groundwaters: a sensitivity study of thermodynamic equilibrium
1036 constants. *Appl. Geochem.* **14**, 907-916.
- 1037 Verney-Carron A., Vigier N., Millot R. and Hardarson B. S. (2015) Lithium isotopes in
1038 hydrothermally altered basalts from Hengill (SW Iceland). *Earth Planet. Sci. Lett.* **411**, 62-
1039 71.
- 1040 Vigier N., Decarreau A., Millot R., Carignan J., Petit S. and France-Lanord C. (2008)
1041 Quantifying Li isotope fractionation during smectite formation and implications for the Li
1042 cycle. *Geochim. Cosmochim. Acta* **72**, 780-792.
- 1043 Vigier N., Gislason S. R., Burton K. W., Millot R. and Mokadem F. (2009) The relationship
1044 between riverine lithium isotope composition and silicate weathering rates in Iceland.
1045 *Earth Planet. Sci. Lett.* **287**, 434-441.
- 1046 Vigier N. and Godd ris Y. (2015) A new approach for modeling Cenozoic oceanic lithium
1047 isotope paleo-variations: the key role of climate. *Clim. Past* **11**, 635-645.
- 1048 Waber H. N., Gimmi T. and Smellie J. A. T. (2012) Reconstruction of palaeoinfiltration during
1049 the Holocene using porewater data (Laxemar, Sweden). *Geochim. Cosmochim. Acta* **94**,
1050 109-127.

1051 Wanner C. and Sonnenthal E. L. (2013) Assessing the control on the effective kinetic Cr isotope
1052 fractionation factor: A reactive transport modeling approach. *Chem. Geol.* **337**, 88-98.
1053 Wanner C., Sonnenthal E. L. and Liu X.-M. (2014) Seawater $\delta^7\text{Li}$ a direct proxy for global CO_2
1054 consumption by continental silicate weathering? *Chem. Geol.* **381**, 154-167.
1055 Wanner C., Druhan J., Amos R., Alt-Epping P. and Steefel C. (2015) Benchmarking the
1056 simulation of Cr isotope fractionation. *Comput Geosci* **19**, 497-521.
1057 Wimpenny J., Gislason S. R., James R. H., Gannoun A., Pogge Von Strandmann P. A. E. and
1058 Burton K. W. (2010) The behaviour of Li and Mg isotopes during primary phase
1059 dissolution and secondary mineral formation in basalt. *Geochim. Cosmochim. Acta* **74**,
1060 5259-5279.
1061 Wolery T. J. (1992) *EQ3/6: Software package for geochemical modeling of aqueous systems:*
1062 *Package overview and installation guide (version 7.0)*, Livermore, California.
1063 Wunder B., Meixner A., Romer R. and Heinrich W. (2006) Temperature-dependent isotopic
1064 fractionation of lithium between clinopyroxene and high-pressure hydrous fluids. *Contrib.*
1065 *Mineral. Petr.* **151**, 112-120.
1066 Xu T., Sonnenthal E. L., Spycher N. and Zheng L. (2014) TOUGHREACT V3.0-OMP
1067 Reference Manual: A Parallel Simulation Program for Non-Isothermal Multiphase
1068 Geochemical Reactive Transport. *LBNL Manual*
1069 [http://esd.lbl.gov/FILES/research/projects/tough/documentation/TOUGHREACT_V3-](http://esd.lbl.gov/FILES/research/projects/tough/documentation/TOUGHREACT_V3-OMP_RefManual.pdf)
1070 [OMP_RefManual.pdf](http://esd.lbl.gov/FILES/research/projects/tough/documentation/TOUGHREACT_V3-OMP_RefManual.pdf).
1071 Yang L. and Steefel C. I. (2008) Kaolinite dissolution and precipitation kinetics at 22°C and pH
1072 4. *Geochim. Cosmochim. Acta* **72**, 99-116.
1073 Zhang L., Chan L.-H. and Gieskes J. M. (1998) Lithium isotope geochemistry of pore waters
1074 from ocean drilling program Sites 918 and 919, Irminger Basin. *Geochim. Cosmochim.*
1075 *Acta* **62**, 2437-2450.
1076
1077